A numerical parametric investigation on the optimal design and operation of coaxial ECR thrusters

Alvaro Sánchez-Villar, Mario Merino and Eduardo Ahedo
Equipo de Propulsión Espacial y Plasmas, Universidad Carlos III de Madrid, Leganés, Spain
alvaro.sanchez.villar@uc3m.es.

KEYWORDS:

Electron cyclotron resonance thruster, modeling, resonant heating, electromagnetic fields simulation.

ABSTRACT:

A coupled plasma transport and electromagnetic wave model of a coaxial electron cyclotron resonance thruster (ECRT) prototype is used to perform a parametric investigation on mass flow rate, microwave power, applied magnetic field strength and resonance location and geometry of the gas injector. Losses are found to dominate thruster performance, and to scale mainly with the energy per particle ratio. Displacement of the resonance within the thruster chamber shows no significant changes in terms of overall thruster performances or electromagnetic properties. In absence of the ECR region, the thruster performances drop significantly, including the power coupling efficiency of the device. However, the simulations show that the plasma can still absorb electromagnetic power in the region that lies within between the critical density and the upper-hybrid resonance (UHR) parametric surfaces. A lower plasma density near the inner conductor of the device opens a short wavelength propagation channel in this region. Radial injection shows enhanced uniformity in stationary neutrals density, which results in enhanced ionization, outperforming the axial injection alternatives. Comparison with experimental measurements reveals the model matches experimental estimations at the nominal operating point but overestimates the prototype optimal operating mass flow rate.

1 Introduction

The Electron Cyclotron Resonance thruster (ECRT) [1–3] belongs to the class of electrodeless plasma thrusters (EPTs). In conventional electric propulsion (EP) devices, electrodes are used to generate the discharge. These components are known to be life-limiting components due to their erosion. EPTs use electromagnetic (EM) heating to ionize and heat the propellant, avoiding the use of cathodes in the design. The operational principles of the ECRT are based on the use of an applied magnetic field, generated by either solenoids or permanent magnets, allowing the propagation and absorption of electromagnetic waves and also the generation of a magnetic nozzle (MN) that expands and accelerates the plasma, creating magnetic thrust.

A recent overview of the history of the development of the ECRT can be found in the introduction of Ref. [4]. In the recently-concluded H2020 MINOTOR project, a novel low power thruster concept that uses a coaxial line to feed microwave power to the discharge was studied. The goal was to improve the understanding of the ECRT operation and to prove the feasibility of this technology, both experimental and theoretically. Several thorough experimental campaigns were performed to optimize the prototype [3, 5–12], and also resulted in significantly refined experimental apparatus. An ECRT simulation model [4] based on this thruster concept was developed and utilized to characterize the plasma discharge of the prototype, providing quantitative estimations of the thruster performances and showing coherence with experimental measurements [5] at nominal thruster operation. Additionally, the model provides support in the optimization process of the thruster design.

This paper shows the results of different parametric investigations performed on the ECRT model of the 30 W prototype being developed at ONERA. Firstly, an analysis of the simulation results at different operating points is shown, comparing to experimental measurements. Secondly, the effects of the ECR zone location is investigated. Finally, a study of the impact of injector location in the thruster chamber is presented.

The rest of the document is structured as follows. Section 2 explains the simulation model, including the definitions of thruster performances used. Section 3 details the effects of the operational parameters, these being the mass flow rate $\dot{m}$ and the forwarded power, on thruster performances, comparing with experimental measurements of the real prototype. Section 4 shows the ECR location investigation. Section 5 details the impact of the injector location. Section 6 gathers the principal conclusions of the manuscript. Appendix A provides a simulation outline and appendix B explains the simulation domain.

2 Simulation model

The axisymmetric model of the ECRT is explained in detail in [12]. Next, only a brief summary of its main features is provided. The model solves the coupled time evolution of the plasma transport and the fast electromagnetic fields, obtaining stationary solutions for both the plasma properties and the EM fields. The plasma transport model [13, 14] uses a hybrid approach, treating the heavy species with a particle in cell (PIC) code with Monte-Carlo collisions (MCC) referred as the I-module here, and the electrons as a magnetized diffusive fluid [14]. This choice is motivated by the considerable computational cost reduction associated to this approach.

Amongst its capabilities, the I-module computes the macroparticles' motion, interaction with the walls including the particle and energy fluxes, and the ionization, excitation, charge-exchange, and Coulomb collisions. Particle-wall interaction models incorporate ion recombination and re-emission as neutrals, neutral mass flow rate $\dot{m}$ injection and a Bohm forcing algorithm at the sheath edge. The PIC module uses a structured cylindrical mesh (PIC-mesh) which simplifies the algorithm and reduces significantly the computational costs.

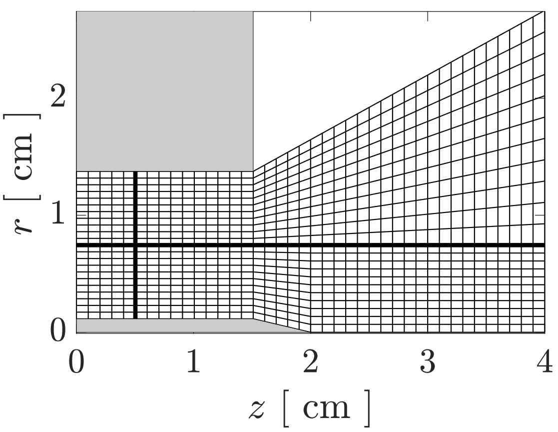

Figure 1: PIC-mesh view with two surfaces of interest for the study highlighted: a transverse cross-section at $z = 0.5$ cm, and a cylindrical section with $r = 0.745$ cm. The magnetic field aligned mesh of the E-module and the unstructured mesh of the W-module are not shown.

The electron-fluid (E-) module computes the solution using a finite volumes method in a B-aligned mesh. The model assumes quasi-neutrality, no electron inertia, isotropic electron pressure and temperature, a diffusive heat flux equation and a phenomenological turbulence based model in the azimuthal direction based on a parameter to be adjusted empirically. The power deposition due to the fast electromagnetic fields appears as a source term in the electron energy equation. The electron module uses the heavy species densities and velocities to compute the macroscopic properties of the electrons. Then, it provides the PIC-module with the electrostatic potential and the electron temperature.

The EM wave (W-) module is a finite element frequency domain full wave model that solves for the electromagnetic fields in the excited plasma using a cold plasma model [15]. The model takes as inputs the electron density and collisionality maps from the E-module and computes the electromagnetic fast fields (i.e. both electric and magnetic fields) and computes the EM power absorption (Q_a) maps.

The code uses a time-marching approach, where for each PIC-module timestep Δt_I, that is set ensuring that the fastest ion particles do not cross more than half a cell of the PIC-mesh per timestep, the E-module is run 10 times. As both the electron density and the effective collisionality vary only slowly as the steady-state is approached, the W-module is only run every 5000 steps. All simulations reported here converge after three W-module updates.

Parameter	Name	Value
L [cm]	Inner rod length	2
r_{rod} [cm]	Inner rod radius	0.115
l [cm]	Lateral wall length	1.51
R [cm]	Lateral wall radius	1.375
L_p [cm]	Plume domain length	2
R_p [cm]	Plume domain radius	2.75
z_{inj} [cm]	Injection surface center z	0.0
r_{inj} [cm]	Injection surface center r	0.5735
t_{inj} [cm]	Injection surface width	0.229
r_c [cm]	Coaxial shell radius	0.3
f [GHz]	Applied EM frequency	2.45
$\dot{m}$ [mg/s]	Neutral mass flow rate	0.2
P_f [W]	Power forwarded	30
Δt_I [ns]	Ion module timestep	$\mathbf{10}$
Δt_E [ns]	Electron module timestep	$\mathbf{0.25}$
u_{inj} [m/s]	Average injection velocity	300
T_{inj} [eV]	Injection temperature	0.02
α [-]	Anom. transport coefficient	0.02
$N_{el,I}$ [-]	PIC mesh's cell number	880
$N_{el,E}$ [-]	MFAM's cell number	807
$N_{el,W}$ [-]	Wave mesh's cell number	96526

Table 1: Geometrical, operational and simulation parameters in the nominal case.

Figure 1 shows the PIC-mesh used in the simulation domain with the geometry of the prototype studied. This mesh is a reduced version of that of [4], allowing faster simulation times. In Appendix B it has been checked that the mesh does not affect substantially the simulation results. Additionally, it shows two surfaces which are used as target locations for the study in sections 3 and 5. Firstly, a horizontal line located at the middle radius (i.e. $r = 0.745$ cm) of the thruster chamber, which allows to investigate trends in the axial direction. Secondly, a radial line of at $z = 0.5$ cm which provides with information of the radial evolution of the plasma properties within the thruster chamber.

Table 1 shows the different geometrical, operational and simulation parameters for the nominal point of operation (i.e. case REF).

The model estimates the overall performances of the thruster as detailed in Ref. [4]. The thrust F of a MN-based thruster is generated partially inside the source, but mainly in the MN region, which extends to infinity. In the present simulation, F is computed by integration of the plasma momentum on the free boundaries of the domain $\partial\Omega_f$,

$$F = \sum_s \int_{\partial\Omega_f} \left(m_s n_s u_{zs} \boldsymbol{u}_s \cdot \mathbf{1}_n + n_s T_s \mathbf{1}_z \cdot \mathbf{1}_n\right) \mathrm{d}S, \quad \text{(Eq. 1)}$$

where the sum on s extends to all species. Since the expansion continues downstream the maximum z of the simulated domain in the remaining part of the magnetic nozzle, the magnetic thrust is underestimated by the simulation. However, most of the ion acceleration in this ECRT was measured to be localized in the first few cm after the thruster chamber exit [16]. The specific impulse is calculated from this magnitude as $I_{sp} = F/\dot{m}$. The microwave power entering the thruster, P_f, is partially absorbed by the plasma, P_a, and partially reflected back through the coaxial cable, P_r, thus

$$P_f = P_a + P_r, \quad \text{(Eq. 2)}$$

and free-space radiation losses are neglected. The reflected power is obtained directly from the voltage standing wave ratio (VSWR) at the coaxial cable, computed as the ratio of the maximum and minimum values of the radial electric field, and is directly related to the power coupling efficiency η_p as

$$\eta_p = 1 - \frac{P_r}{P_f} = 1 - \left(\frac{\text{VSWR} - 1}{\text{VSWR} + 1}\right)^2. \quad \text{(Eq. 3)}$$

Low coupling means high power reflection, so that there is a significant impedance mismatch between the line and the thruster, which would require specific impedance matching in the circuit design. Regarding the balance of power it can be split into several terms:

$$P_a = P_{exc} + P_{ion} + P_{wall} + P_p, \quad \text{(Eq. 4)}$$

where P_{exc} and P_{ion} are the power spent in excitation and ionization collisions, P_{wall} is the sum of kinetic, thermal, and heat flux power lost to the walls, and P_p is the power flux of all species through the free boundaries. Consequently, we can define the loss ratios $\epsilon_{exc} = P_{exc}/P_a$, $\epsilon_{ion} = P_{ion}/P_a$, and $\epsilon_{wall} = P_{wall}/P_a$.

The (overall) thruster efficiency is computed as

$$\eta_F = \frac{F^2}{2\dot{m}P_a}. \quad \text{(Eq. 5)}$$

This efficiency can be approximately decomposed as

$$\eta_F \approx \eta_u \eta_e \eta_c \eta_d = \frac{\dot{m}_{i\infty}}{\dot{m}} \frac{P_p}{P_a} \frac{P_i}{P_p} \frac{P_{zi}}{P_i} \quad \text{(Eq. 6)}$$

where $\eta_u = \dot{m}_{i\infty}/\dot{m}$ is the utilization efficiency, i.e. the fraction of propellant mass flow rate that reaches the domain free boundaries as ions ($\dot{m}_{i\infty}$); $\eta_e = P_p/P_a$ refers to the energy efficiency, i.e. the fraction of absorbed power that becomes plume mechanical and thermal power (P_p); $\eta_c = P_i/P_p$ is the conversion ratio, defined as the portion of the plume power in the form of kinetic ion power (P_i); finally, $\eta_d = P_{zi}/P_i$ is the divergence efficiency, which is the fraction of ion kinetic power which is axial (P_{zi}), and thus generates thrust.

Observe that the estimation of the thrust efficiency η_F with right hand side of Eq.6 neglects the contribution to thrust of both neutrals and electrons. While the latter is negligible after full conversion into ion power, it is still not negligible at the end of the simulation domain used here. The presence of significant electron temperatures and densities and the end of the domain lead to electron contributions to total thrust of around 25 %. A MN model would be required in order to obtain a fully developed plume.

Additionally, another relevant ratio of ion flow rate at the free boundaries with respect the total at all the simulation boundaries:

$$\eta_{prod} = \frac{\dot{m}_{i\infty}}{\dot{m}_i}. \quad \text{(Eq. 7)}$$

3 Operating parameters

This section focuses on the effect of variations of the mass flow rate and the forward power with respect to the nominal operating point (represented by simulation REF of appendix A). The new simulation cases are M0 and M2, which feature a 25% lower and higher mass flow rate with respect to the nominal case, respectively, and cases P0 and P2, which have half and double the nominal microwave power forwarded, respectively. All the other input parameters of the simulations are set to nominal. The forward power P_f is chosen as a parameter of analysis rather than the absorbed power P_a to assess the changes in the power reflection ratio. It has been checked that the analysis based on varying

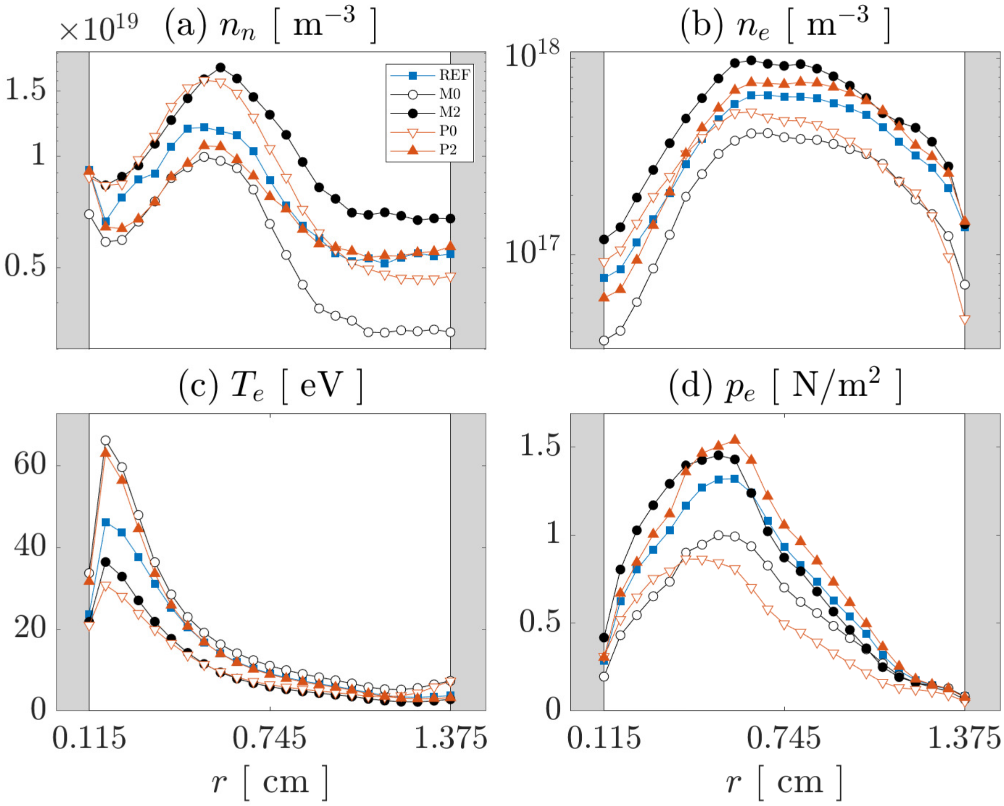

Figure 2: Radial evolution of (a) the neutrals density, (b) electron density, (c) electron temperature, and (d) electron pressure, for multiple operating conditions.

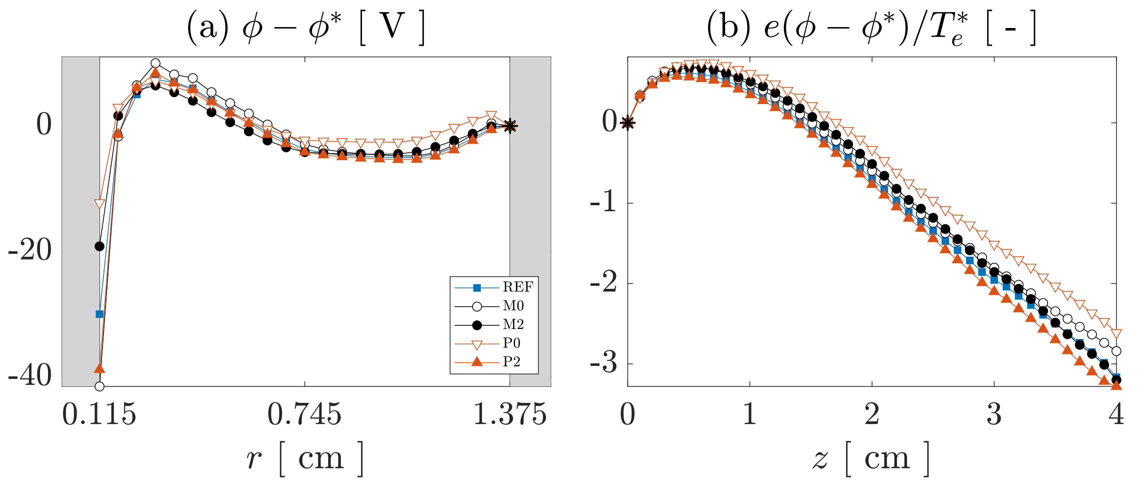

Figure 3: Effect of the operating point on (a) the axial and (b) the radial evolution of electrostatic potential. Radial values take as reference the value at the lateral wall (i.e. $r = 1.375$ cm). Axial values are normalized taking the backplate as reference, being T_e^* = 7.9, 9.6, 5.1, 5.6, and 7.6 eV for cases REF, M0, M2, P0 and P2, respectively.

P_a instead reveals similar trends as those reported here.

Fig. 2(a) shows that the general effect of an increase in $\dot{m}$ is to monotonically rise the neutrals density in the chamber, with such correlation not being directly proportional. Physical processes as propellant ionization, ion recombination at the walls and expansion from the injected region are affected by the mass flow rate itself. Depletion of neutrals density towards the lateral wall is highly influenced by this parameter.

The trend with forwarded power is less clean-cut, showing that in the bulk of the discharge the density of neutrals varies inversely to the changes in forwarded power, except for the region close to the lateral thruster wall where small variations are observed. Additionally, this correlation is not of direct proportionality, as a decrease in power has a greater impact in the resulting neutrals density. A possible explanation relies in the fact that optimal levels of ionization at this thruster configuration are achieved at the nominal case, reducing the efficacy of an increase in P_f on the ionization.

The dynamics of electrons interacts strongly with many physical phenomena. Figure 2(c) shows the radial evolution of the electron temperature for different operational points, exhibiting greater changes in the region close to the inner rod surface, which is the region of maximum power absorption for all cases. In fact, as it is shown in Fig. 4(b)-(f), the power absorption density maps remain barely affected by the varied parameters, only applying a scaling in the magnitude in the cases with different P_f. The electron temperature in stationary conditions, increases with P_f and decreases with $\dot{m}$ as would be expected from the energy per particle/mass. The higher T_e values near the inner conductor and the strong temperature gradient are a robust result obtained in all the simulations, which can be explained by the dominance of this term in the electron internal energy equation.

Regarding the electron pressure, shown in Fig. 2(d), it increases in the entire domain both with mass flow rate and forward power. While increasing mass flow rate enhances electron pressure closer to the inner rod, increasing the forward power enhances the electron pressure mainly in the center of the annular chamber, away from the either wall. Regarding the drop in electron pressure close to the inner rod surface compared to case M2, it is a result of the electron density depletion in the vicinity of the inner rod for increasing P_f, as it is mentioned later. The pressure value at the walls is essentially unaffected by these variations, and as a consequence, increasing either the mass flow rate or the power results in steeper radial gradients.

Lastly, figure 2(b) shows variations experienced by electron density. While these variations can be inferred directly from those of the electron temperature and pressure, it is worth discussing electron density due to its more complex behavior. As expected the plasma density increases with both the mass flow rate and the forward power. This is related to ionization being the primary factor affecting the electron density in stationary conditions, and ionization is driven by mass flow rate and forward power.

However, while increasing mass flow rate enhances electron density everywhere, increasing the forward power enhances the electron density mainly at higher radii, away from the inner rod element of the thruster. In fact, the electron density close to the inner element is seen to decrease slightly with the forward power, so that a steeper radial gradient arises.

The changing plasma density map also leads to significant changes in EM power propagation and absorption inside the thruster. This is because of the appearance of a new propagation region close to the inner element when the electron density there is sufficiently low, and can be understood as a channel or “tube” for EM power propagation, as shown in Fig. 4.

Figure 3(a) shows the effect of both mass flow rate and forward power on the radial evolution of the electrostatic potential, taking as reference the potential at the lateral wall. Note that for increasing mass flow rate, the radial evolution of the potential, and thus the radial electric fields are almost unaffected in the bulk of the plasma. The main difference is the increase in the potential drop at the inner rod surface, explained by the increase in electron temperature there with decreasing mass flow rate. The normalized behavior of the radial electric fields is again very similar for different forward powers. The main differences are that the potential is higher close to the lateral wall for lower forward powers as there the electron temperature is greater, and the higher radial electric field at the inner rod surface for higher forward powers. The latter effect is again linked to a higher electron temperature near the inner wall, the higher the forward power.

Figure 3(b) shows the axial evolution of the plasma potential along z (i.e., essentially in the parallel direction) on the mid-radius of the thruster chamber, for the different operating conditions considered in this study. The electrostatic potential values are normalized with a reference potential and electron temperature, taken as the backplate node, indicated by the marker $*$ to facilitate line comparison. This normalization shows that the studied variations keep essentially the same axial profiles.

Both the mass flow rate and the forward power, by affecting the equilibrium state of the plasma transport properties, specifically the electron density and collisionality, alter significantly the propaga-

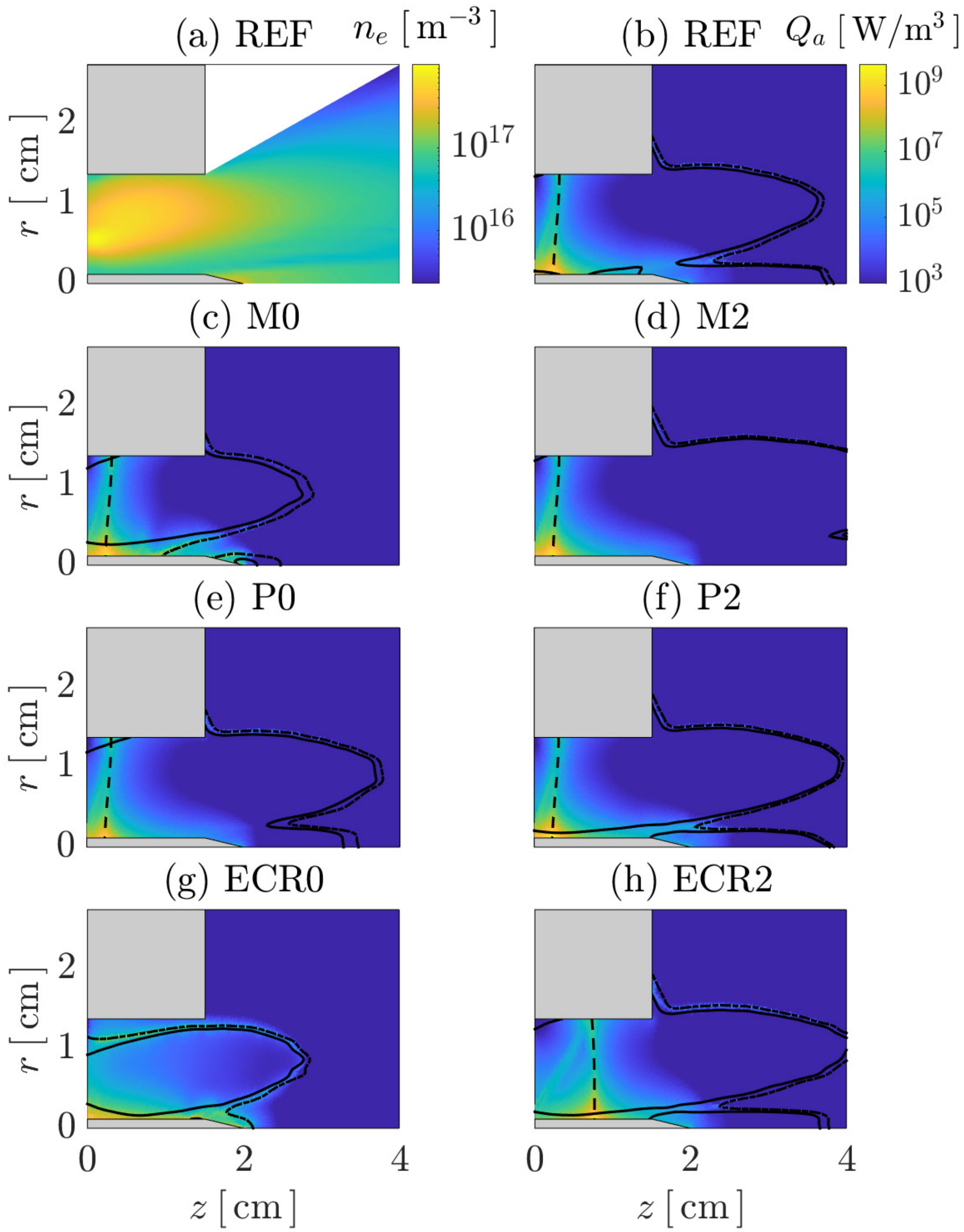

Figure 4: The first row shows the plasma density and power absorption map for case REF. Figures (c)-(f) show the power absorption density maps for cases M0, M2, P0, P2, ECR0 and ECR2. Lines represent the ECR (dashed), the critical density loci (solid), and the UHR (dash-dotted).

tion regimes present in the thruster. This modifies the paths through which the electromagnetic power flows and reflects and even the resonant surfaces where these are absorbed. Since the collisionality is strongly dominated by the anomalous contribution in the simulations shown and this depends on the magnetic field, it is the electron density that varies the most across simulations.

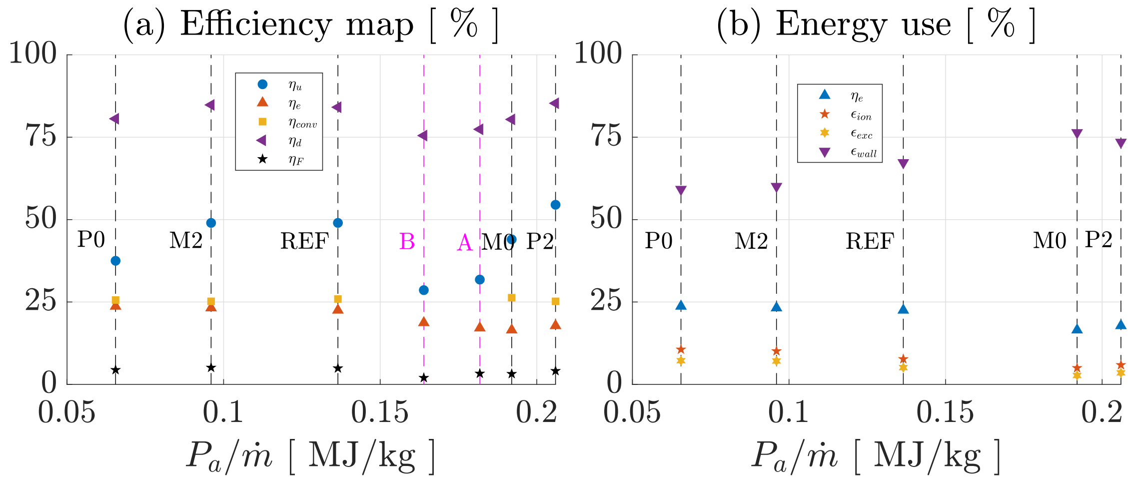

Figure 5: Map of efficiencies and energy use for the cases shown in the parametric investigation of forward power and mass flow rate. In the horizontal axis the $P_a/\dot{m}$ represents the energy absorbed per mass, or particle. For the sake of comparison, in (a) two experimental operational points (A and B) reported in Ref. [10] are shown.

In this thruster configuration, several parametric surfaces appear that represent specific conditions of the plasma density and/or applied magnetic field intensity for which there is either a cutoff of an specific propagating electromagnetic wave mode or a resonance. Figure 4(b)-(f) shows the power absorption maps for all thruster operating points considered, including their corresponding parametric surfaces. Dashed lines represent the location of the ECR, static in this section as it depends on the B_0 and ω. Solid and dashed dotted lines represent the location of the cutoff of the parallel mode, which occurs at the critical density (i.e. density at which the excitation frequency is that of the plasma), and the upper hybrid resonance (UHR). Both surfaces are affected by the electron density.

Power absorption (Q_a) maps resemble each other having the region of maximum power absorption located at the location of the ECR and close to the inner rod surface as explained in [4], thus supporting the robustness of the model. The maximum Q_a increases with increasing forward power, while keeping the shape similar. The electromagnetic power accesses from the dielectric window (i.e. interface of the coaxial with the thruster chamber). Then it propagates and most EM power is absorbed in the ECR region. Downstream of the ECR region, an evanescent region for all EM wave modes is dominant in most of the plasma. As the plasma density follows the mass flow rate in the entire domain, the result of changing the thruster operating point is to displace the parallel mode cutoff loci and the UHR, downstream for increasing mass flow and upstream for lower mass flow. This effect can also be noticed in the case of changing forward power, although it is less evident.

Additionally, as a result of the steeper electron density depletion close to the inner rod surface for higher forward power, a propagation channel opens for increasing forward power, and contrary occurs in the case of increasing mass flow rate, as the electron density close to the inner rod increases as well. This propagating region allows to deposit some EM power downstream the ECR region.

This channel opening has an effect in the coupling efficiency η_c reported in Tab. 3, as for increasing mass flow rates it decreases from 96.1% to 80.0%, and for increasing forward power increases from 87.6% to 91.6%.

Table 3 shows all the different performance parameters for all the cases investigated. As expected the thrust increases with both mass flow rate and forward power. However the sensitivity to changes in these parameters is greater in the decreasing direction. In the case of the overall thruster efficiency, while in terms of forward power the operational point of the thruster is close to the optimum, the mass flow rate allows for slight increases. Case P2 denotes that for further increase of the forwarded power, although the utilization efficiency is increased by the increased electron temperature within the thruster chamber, the added power results in rising the heat losses through the walls. For increased mass flow, the utilization remains unaffected but the losses are significantly decreased. This denotes that the optimal thruster operating point is for slightly higher mass flows and similar forward power. The model suggest that the main form of efficiency losses are losses to the walls. This is true for all simulations in this work. Clearly, any improvements to this thruster technology must address the reduction of wall losses to enhance thruster efficiencies.

Figure 5(a) shows the variation of the different thruster efficiencies with the ratio of mass flow rate to absorbed power. Two operational points measured in an experimental campaign reported in Ref. [10] are also added for the sake of comparison. It can be noted that only the energy efficiency and the utilization efficiency follow a trend with the $\dot{m}/P_a$ ratio, the former increasing and the latter decreasing with it, as measured experimentally [10]. The overall thruster efficiency exhibits a maximum relatively close to case REF.

Figure 5(b) details the computed different energy uses given to the absorbed power. As mentioned before, the energy lost to the wall decreases with the amount of mass flow rate per unit absorbed power. Furthermore, both ionization, excitation and energy ratios increase with decreasing $P_a/\dot{m}$. However, the curves saturate at values between case M2 P0, where no significant changes can be noticed. This implies that there is an optimum in P_f in this type of thruster and it is slightly to higher mass flow rates and lower forward powers than the nominal operation point. Beyond that point, increasing the forward power or reducing mass flow rate would result in larger wall losses, and more inefficient operation.

Comparing the experimental values with the model estimations, it is noticed that cases M0 and A denote comparable performances in overall thruster, utilization, energy and divergence efficiencies, for similar operational points. However the simulation model overestimates the utilization efficiency. The conversion ratio to ion power is seen to be far from 1 in the present simulations. Unfortunately, at this time the experimental cases provide no information about their conversion ratios to afford a direct comparison or validation in this respect.

We note that case B exhibits a significant decrease in performance with the ratio $\dot{m}/P_a$ which is not estimated by the envelope of cases run in this investigation. This suggests either an overestimation of the optimal ratio $\dot{m}/P_a$ for the coaxial ECRT model presented here with respect to the experiments.

4 ECR location

The operation of the ECRT relies in the electromagnetic power deposition that takes place mainly in the ECR region. In this section, an investigation on the influence of the location of the ECR region is performed. Using the nominal case (i.e. REF) as reference, we have scaled up and down the strength of the applied magnetic field $\boldsymbol{B}_0$ to displace the ECR resonance in the original device. Two alternative locations of the ECR region with respect to the nominal have been investigated:

- ECR0: decrease the applied magnetic field intensity by a 20%, thus moving the ECR resonance upstream and outside of the discharge chamber. In this case we have forced the thruster to operate without ECR region to check whether its operation is feasible and to understand the mechanisms of power deposition in this case.
- ECR2: increase the magnetic field intensity by a 25%. This case enables studying the effects of moving the ECR region further downstream.

Figure 6 shows the location of the ECR regions for the two alternative cases and the nominal case, representing in the background color the nominal applied magnetic field. The cyan curve in Fig. 6 shows the location of ECR region for case ECR0, in REF the location of the nominal ECR region (i.e. REF) and finally, in magenta the ECR location corresponding to case ECR2.

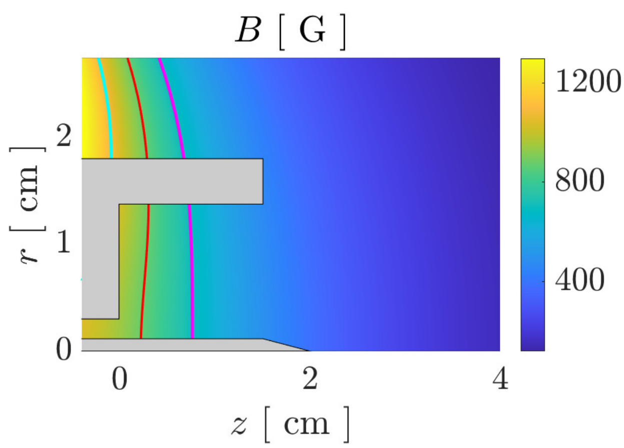

Figure 6: Resonance locations analyzed in the study. The applied magnetic field intensity of the reference case is shown in the colormap. The contour lines represent the three ECR locations investigated: red (nominal), cyan (behind backplate) and magenta (downstream).

Note that since the excitation frequency has not been varied in any case, the location of the ECR region is still located at the 875 G contour line, although the location of this contour line differs for each case. As a consequence of varying the magnetic field strength, the magnetization of charged particles and thus the transport coefficients vary among simulations. However, this is seen to play only a minor role in the present simulations. Indeed,

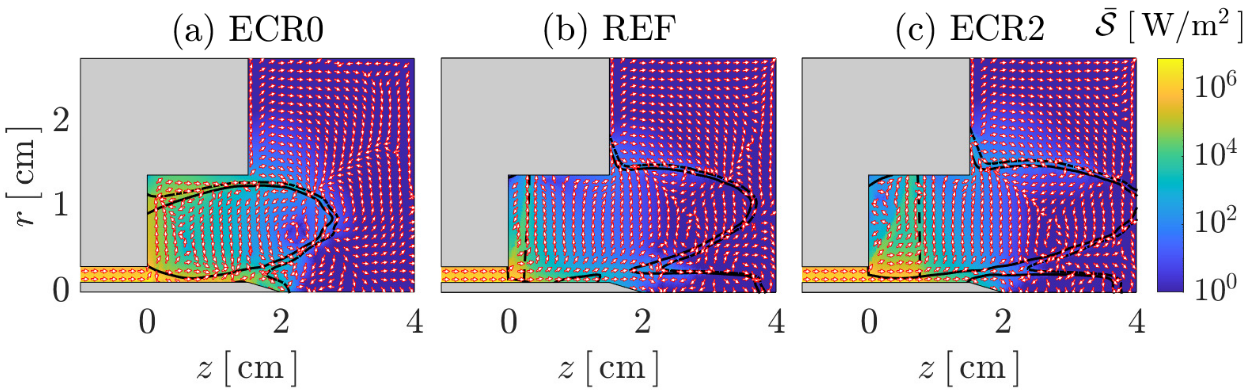

Figure 7: Poynting vector representation for cases (a) ECR0, (b) REF and (c) ECR2, with colormap indicating its magnitude, and the arrows its direction and sense. Lines represent the ECR (dashed), the critical density loci (solid), and the UHR (dash-dotted).

the main change in the plasma response is due to the effect on wave propagation and absorption that shifting the position of the ECR resonance has.

Figures 4(g) 4(a) and 4(h) show the power absorption maps for cases ECR0, REF and ECR2, respectively. Comparing the three cases, those with an ECR region (i.e. REF and ECR2) absorb most of the power there, and a small part of the absorption takes place close to the propagating channel and at the UHR.

Case ECR0 shows the importance of the ECR in ECRT technology, as it eliminates the ECR from the domain, and therefore EM power propagation and absorption behaves differently. In principle one could expect that this configuration does not absorb EM power. However, there is significant power absorption concentrated both at the propagating region close to the antenna, and at the UHR.

Figure 7 plots the time average of the Poynting vector $\bar{\boldsymbol{S}} = \frac{1}{2}\operatorname{Re}\{\tilde{\boldsymbol{E}} \times \tilde{\boldsymbol{H}}^*\}$, where $\tilde{\boldsymbol{E}}$ and $\tilde{\boldsymbol{H}}^*$ are the complex amplitude electric field vector and the complex conjugate of the complex magnetic field, respectively. $\bar{\boldsymbol{S}}$ represents the time average flux of electromagnetic energy through the domain. Note that this represents the net flow of power in steady state conditions, including any reflected power. Figs. 7(a), 7(b) and 7(c) show the Poynting flux magnitude in the colormap and the direction in arrows. These figures detail the different paths of propagation of the electromagnetic power through the thruster for different ECR locations. In all cases the power accesses through the coaxial cable, where the Poynting intensity is the largest. From this point on, the EM power flows mainly close to the inner rod surface in all cases through the propagating channel. As detailed before, this channel appears due to the density depletion close to the inner rod surface.

In all cases, there is a clear correlation between the presence of resonances and cutoffs and the Poynting flux vector. Resonances as the ECR or the UHR, are boundary surfaces that act as regions of power absorption. In fact, the power absorption is coherent with the behaviour of the $\bar{\boldsymbol{S}}$ vector as it crosses a resonance. $|\bar{\boldsymbol{S}}|$ decreases as $\bar{\boldsymbol{S}}$ flows through the resonance. This effect can be easily noticed in the cases with an ECR (i.e. REF and ECR2). All resonances absorb EM power from the normal component of $\bar{\boldsymbol{S}}$. As a direct consequence, as considerable fraction of the normal component is absorbed, and $\bar{\boldsymbol{S}}$ tends to become tangential to the resonances. In any case, in all the discharges the UHR behaves as a stopper for EM propagation downstream the plasma bulk. Furthermore, $\bar{\boldsymbol{S}}$ starts to bend even before the resonance, becoming tangential progressively. This is a direct consequence of the damping included in this model (in this case collisional), as it increases the resonance thickness [17]. Again, although this effect is more evident in the ECR than in the UHR (see cases REF and ECR2 in Figs. 7(b) and 7(c)), it occurs at both, as can be seen in case ECR0, Fig. 7(a).

Cutoff parametric surfaces also modify the propagation of EM power. These boundary surfaces limit part of the propagating EM power across them, and only a small fraction can tunnel through. Specifically, Figs. 7(a) and 7(b) show a black solid line, which denotes the location of the critical density $n_{cr} = \epsilon_0 m_e \omega^2/e^2$, being ϵ_0 the vacuum permittivity, and m_e and e the electron mass and charge. This surface separates the so-called underdense plasma (i.e. $n_e < n_{cr}$) from the overdense plasma (i.e. $n_e > n_{cr}$. In particular, for $\omega_{ce} < \omega$ and overdense plasmas (that is in the region inside the solid black line) all electromagnetic modes are evanescent. Therefore, $|\bar{\boldsymbol{S}}|$ decays exponentially in this region.

In all cases, the electromagnetic energy is able to tunnel through the evanescent region. However, in case ECR0 this effect is more evident close to the backplate, as the perfect electric conductor boundary condition imposed on the backplate forces the wave electric field to be normal. This combined with a dominant azimuthal wave magnetic field leads to a radial Poynting vector. Such effect is not noticed in the cases with ECR resonance, as the Poynting vector reaches the outer conductor through a diagonal propagating path (see Figs. 7(b) and (c).

Comparing the three different scenarios we note that the coupling efficiency of case ECR2 is enhanced with respect to case REF, increasing from a 91.1% to a 98.2 %. However, case ECR0 exhibits a strong reflection and slow coupling efficiency, in this case of 18.1%, resulting in only 5.42 W of absorbed power. This indicates that the presence of the ECR resonance is essential for an efficient power coupling with the plasma in the thruster.

Overall, displacing the ECR resonance further downstream or upstream shows no significant effect in thruster performances, as long as it remains in the plasma. However some small modifications can be noticed. The increase in the utilization efficiency for case ECR2 (from 49 to 52%), the decrease in η_e from 22.5 to 19.2% and the increase in P_a from 27.3 to 29.5 W, results in lower overall thruster efficiency of the thruster, that decreases from 4.9 to 4.4%. The main motivation in the decrease of η_e is the increase in the amount of losses to the walls, ϵ_{wall}, that is increased with respect to the reference case. This could be explained by an increased cross-field transport modeled by both the turbulence-based force and heat flux, which is proportional to the applied magnetic field intensity. Note that the latter is increased from case REF to ECR2 by a 25%. Moreover, the production efficiency is higher for the UHR, then the ECR2 and the lowest is at the nominal case. Thus cases ECR0 and ECR2 have a decreased fraction of ions generated that are lost at the walls by recombination, and in principle would increase the losses.

Regarding case ECR0, the power reflection is too large, which decreases substantially the absorbed power (coupling efficiency 18.1% with respect to the nominal 91.1%). While it is clear that this case has lower performance, the effect of removing the ECR is less deleterious than would be expected, reaching a thrust efficiency of 2.7%. The performance of case ECR0 is hindered by a poor utilization efficiency which can be a result of such a high $\dot{m}/P_a$ ratio. Overall, the main inconvenience of this design is its low coupling efficiency.

5 Injector orientation

In this section we show the effects of varying the injector geometry, as detailed in Table 2, with two alternatives: (*i*) Case INJZ0: the injector is displaced to lower radius, and still at the backplate, (*ii*) Case INJR: displace the injector to the lateral wall, close to the backplate, and inject the mass flow rate radially inwards. In this case we have increased the width of the injector port.

Parameter	Units	REF	INJZ0	INJR
z_{inj}	cm	0.0	0.0	0.4
r_{inj}	cm	0.5735	0.35	1.375
t_{inj}	cm	0.229	0.229	0.429
$\boldsymbol{n}_{inj}$	-	$\mathbf{1}_z$	$\mathbf{1}_z$	$-\mathbf{1}_r$

Table 2: Injector geometrical parameters.

Table 2 shows the variety of injector geometries used in this study, characterized by: (*i*) the coordinates of the injection surface center z_{inj} and r_{inj}, (*ii*) the injection surface width t_{inj}, and (*iii*) the injector surface normal vector $\boldsymbol{n}_{inj}$.

The location of the injector affects mainly the maps neutrals density within the thruster chamber. This, in turn, drives the dynamics of the plasma. Comparing the resulting stationary neutral plasma density maps of cases REF and INJZ0, shown in Figs.8(a) and 8(b), it can be noticed that the only noteworthy change is that the radius of the maximum n_n relocates following the injector location. The injected particle flux depends on the mass flow rate and the surface. The magnitude of the maximum is increased in case INJZ0 with respect to case REF since the injector surface is reduced with this modification. This results in a greater injected particle flux, and that for a fixed injected population velocity and temperature, leads to increased neutrals density.

Contrary to case INJZ0, significant changes can be noticed in the plasma properties of the discharge for case INJR, shown in Fig. 8(c). For instance, the behaviour of n_n is completely modified. In this case, the maximum neutral density decreases (from 5 and 8 $\times 10^{19}$ to approximately 2 $\times 10^{19}$ m^{-3}), provided the greater surface area of the injector now located at the lateral wall. Additionally, the resulting map of neutral density is much more homogeneous than the other two, and the average value is significantly higher than what could be expected from the increase in the injector area.

In order to discern the details inside the thruster chamber to a greater degree, the effect of injector geometry in the radial profile of the neutral density at $z = 0.5$ cm is shown in Fig. 9(a). Note that the average neutral density is much larger for case

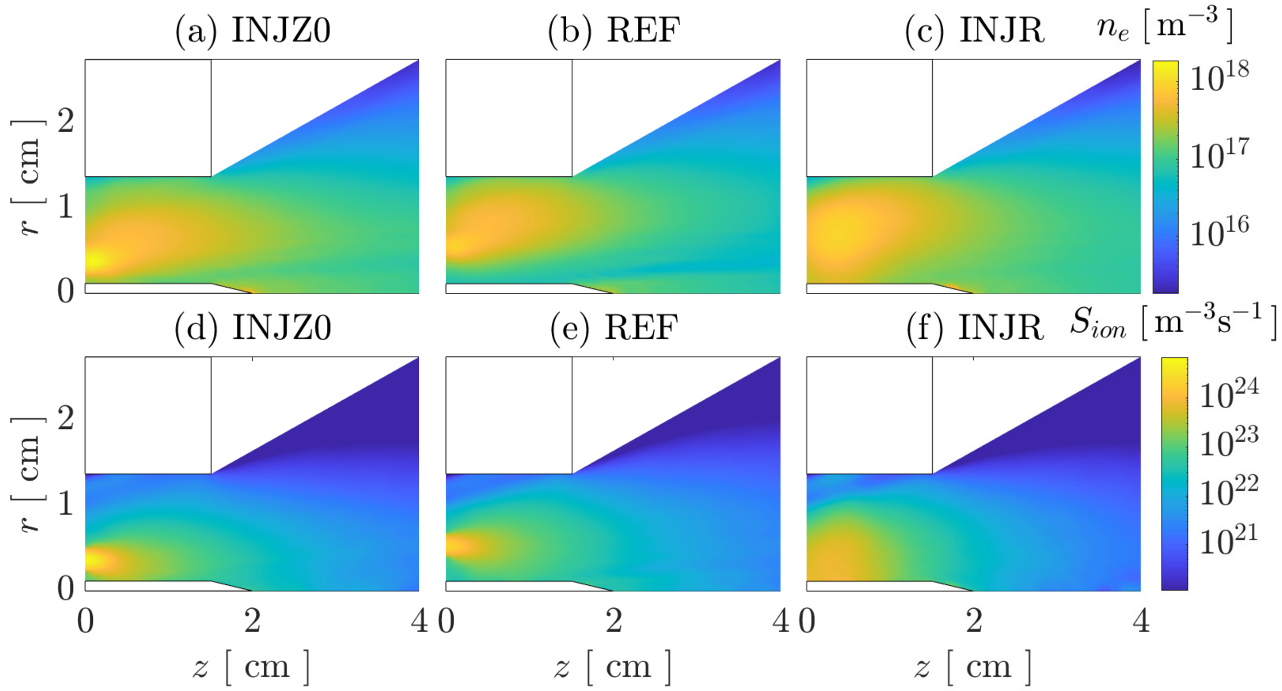

Figure 8: Figures (a), (b), and (c) show the neutral density maps, and (d), (e), and (f), the ionization source maps for different injector geometries.

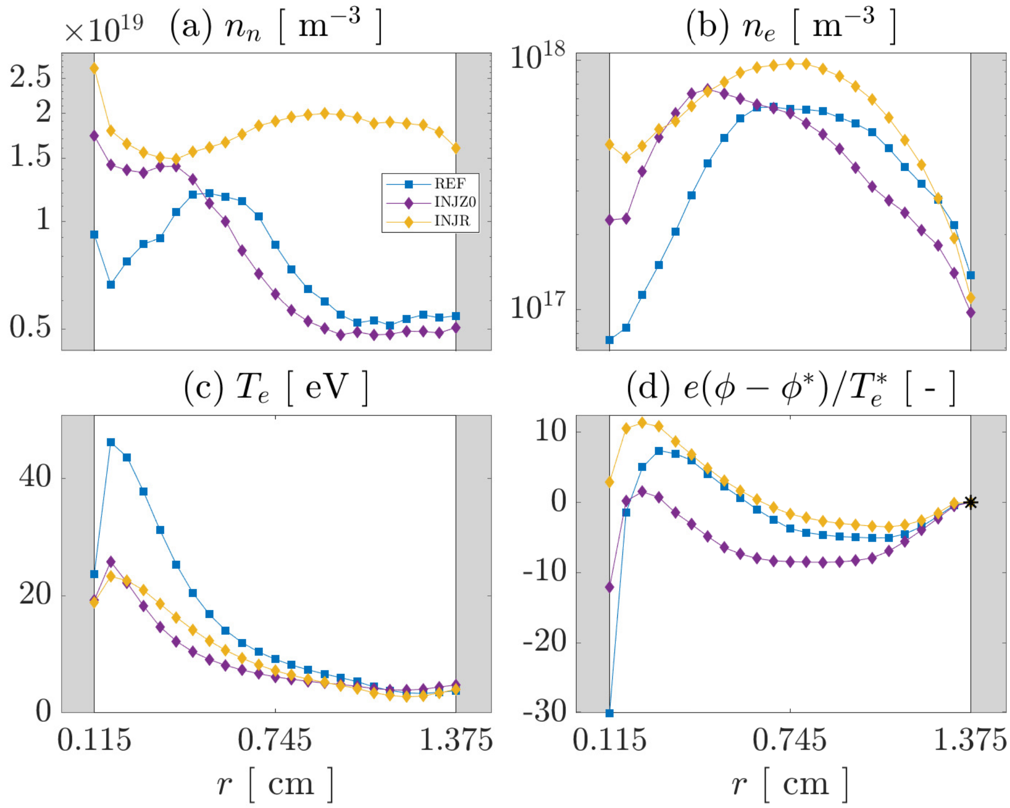

Figure 9: Radial evolution of (a) the neutrals density, (b) electron density, (c) electron temperature, and (d) electron pressure, for different injector locations.

INJR than that of the other two cases, and that for case INJZ0, the density of neutrals is increased towards the inner rod surface with respect to case REF. Additionally, the radial profiles show the previously mentioned enhanced homogeneity of neutral density profiles for case INJR. Furthermore, in all cases the effects of ion-wall recombination at the walls can be noted, being the effect the most significant for case INJR and the least for INJZ0.

Amongst all the simulations shown in this investigation, the injector orientation induces the most significant changes in plasma density. Overall we note that the level of plasma density achieved in case INJR is much greater than for the other two cases, being the lowest that of the nominal injection, see Fig. 9(b). Similarly to the neutrals density, the effect of moving the injector to lower radius along the backplate results in displacing the radius where the peak plasma density is located in that same direction, reaching much greater plasma densities close to the inner rod surface (from approximately 0.8 to 2 $\times 10^{17}$ m^{-3}). Thus, the density depletion that occurs towards the inner rod is prevented, produced by a significantly enhanced ionization in this region. This effect can be noticed in Figs. 8(d) and 8(e), which represent the ionization source term $S_{ion} = n_e \nu_e^{ion}$ for cases INJZ0 and REF. Comparing case INJR to the other two, the effect is to increase the average electron density within the chamber and also replenishing the region close to the inner rod. This is a result of the ionization rate close to this region, which is significantly increased as the amount of neutrals is drastically raised whilst the electron temperature is still above the ionization energy. This effect can be noticed comparing 8(d) and 8(e), to 8(f).

Figure 9(c) shows the effect of injector geometry in the electron temperature and plasma potential. Regarding the radial profile of the electron temperature, we note that the maximum temperature is achieved close to the inner rod surface for all the cases but that its magnitude is doubled for case REF with respect to the other two. Additionally case INJR exhibits a more homogeneous electron temperature than the other two close to this maximum. Moreover, all cases evolve similarly towards the lateral wall, reaching approximately the same T_e there.

In the case radial electrostatic fields (see Fig. 9(d)) we note that there are significant changes between the cases. Although close to the inner rod there is a negative radial electric field for all cases, there is a significant variation in their magnitude. This can be explained due to the differences in the electron temperature and density obtained close to this region for all cases. Close to the inner rod, electron pressure and electrostatic forces balance each other. As the temperature drop is much greater for case REF than for the other two, and the pressure drop is much greater for this case the electron density has to decrease faster towards the inner rod. However, in order to fulfil electron momentum balance, the increased electron pressure force has to be compensated with an increased electrostatic force. As the electron density decreases, the electric potential needs to drop significantly more for case REF than for the other two. Notwithstanding this difference, the radial electric fields are mild in the thruster core, and evolve similarly towards the lateral wall.

Comparing the overall performances of case INJZ0 with respect to the nominal design for the injector, no significant advantages in terms of performance are found. In fact, an equivalent operational point of the nominal design (i.e. M2) provides with similar performances. This case exhibits lower absorbed power with respect to case REF, as the power coupling is significantly decreased. This explains the drop in the maximum electron temperature and may explain the decreased wall losses for this injector configuration, together with the lower radial electric field towards the inner rod exhibited in this case. The temperature drop results in decreased overall level of ionization.

However, the case of radial injection is completely different. We note that a modification in the radial injector leads to improved overall thruster efficiency of a 20% relative to the nominal case, from 5.1% to 6.2%. This is a result of the improvements obtained with the use of a radial injection in the energy, utilization, divergence and conversion efficiencies. Table 3 shows that for case INJR, the resulting wall losses are significantly decreased, from a 67.3% of case REF, to a 56.9%. This is a result of enhanced usage of energy, increasing the ionization and excitation losses and also that provided to accelerate the different species, represented by the energy efficiency. As a result we can conclude that radial injection outperforms the axial injection alternatives.

6 Conclusions

In this work a simulation model of the coaxial ECRT has been used to analyze the effects of different thruster operating points and modifications in the thruster design, such as the ECR region location and the injector orientation. The main findings regarding the neutral and plasma dynamics in the discharge chamber and the near plume region, as well as the EM wave propagation and absorption, have been discussed.

Most scaling with the operating parameters P_a and $\dot{m}$ is well understood and agrees with existing expectations. The plasma profiles and thruster performances depend mainly on the energy per particle, $P_a/\dot{m}$. The main difference relies in the appearance of an EM propagation channel due to plasma density depletion close to the inner rod. The effect is stronger for higher powers than for lower mass flow rates.

In all simulations carried out the main loss mechanism are the wall losses, which eat up most of the potential performance of the device. These losses are seen to scale mainly with the energy per particle ratio. Clearly, this should be a main area of improvement in future ECRT studies.

The central role of the ECR region in power delivery is evidenced by the drastic drop in coupling efficiency when this region is taken out of the simulation domain.

An adequate gas injector design can have a major effect on the neutral density map and consequently affect the plasma production in the thruster chamber, with a direct impact on the thruster performances.

Further work must include a more thorough comparison with additional experiments with more recent versions of the prototype, enabling a more complete validation of the model.

Appendix A: Simulation outline

- CASE EXT: simulation of the ECR thruster with extended simulated domain. The extension reaches 6 cm axially and 4.125 cm radially. Transport simulation domain includes the top plume that extends from the last applied magnetic field line exiting the thruster chamber to the maximum radius of the domain. Simulation includes both singly-charged to doubly-charged ionization, and doubly charged ionization.
- CASE I2: In this simulation the plume is truncated close to the thruster. Modifications are summarized in section Appendix B. The simulation domain extends 4 cm axially and the top plume has been removed. CEX collisions have been deactivated. Both PIC-mesh and MFAM have been coarsened. The timestep of ions and electrons has also been increased.
- CASE REF: This case is the so-called reference case which has been use as the nominal simulation to vary parameters to perform this parametric analysis. Compared to I2, only double ions have been deactivated.
- CASE M0: Case REF with injected mass flow rated modified to 0.15 mg/s.
- CASE M2: Case REF with injected mass flow rated modified to 0.25 mg/s.
- CASE P0: Case REF with injected electromagnetic power modified to 15 W.
- CASE P2: Case REF with injected electromagnetic power modified to 45 W.
- CASE ECR0: Case REF with a scaling factor used in the applied magnetic field intensity, $B_{factor} = 0.8$ so that the ECR is located behind the thruster backplate (see Fig. 6).
- CASE ECR2: Case REF with a scaling factor used in the applied magnetic field intensity, $B_{factor} = 1.25$, displacing the ECR slightly downstream (see Fig. 6).
- CASE INJZ0: Case REF with injector port (still at the back plate) moved towards the inner rod, closer to the applied magnetic field line exhibiting maximum electron temperature in the thruster (see details at Tab. 3).
- CASE INJR: Case REF with injector port located at the lateral, close to the backplate (see details at Tab. 3).

Appendix B: Truncated simulation domain

In this work, the simulation case shown in Ref. [4] has been taken as a starting simulation, defined as extended domain (EXT). Different simplifications have been applied to the simulation setup in order to optimize computational costs of this parametric investigations while checking the relevance of various effects.

Firstly, CEX collisions have been disregarded from the simulation as the associated losses were found to be negligible.

Secondly, the maximum length and radius of the simulation domain have been reduced to twice the characteristic scales of the thruster geometry in order to quantify the importance of boundary effects and reduce computational costs. As a result there is a drop in the thruster performances but qualitatively the thruster performance is maintained. Future research will extend the domain length.

Third, the top part of the near plume above the last magnetic field line exiting the thruster chamber was eliminated from the transport domain simulation due to (*i*) insufficient amount of particle reaching cells in this region required higher overall amount of particles per cell, thus slowing down the simulations, (*ii*) the negligible interaction between this region and the plume. This section of the domain was eliminated only from the plasma transport simulation domains, as the effect of boundary conditions in the electromagnetic problem would not be adequate, and would result in wide differences with respect to those obtained with the EXT domain. At the truncated region, the plasma properties were linearly extrapolated from the values within the transport simulation domain.

Fourth, the axial and radial resolution of both the PIC-mesh and the MFAM is reduced. Given that the cells are coarsened, the timestep was increased thus keeping the condition that the fastest ions do not cross more than one cell per timestep.

Fifth, the effect of doubly-charged ions was disregarded to verify their importance in current simulations. Given that its major effect was found to be a decrease of about 15% on T_e, as a dedicated list for this species required additional computational cost, it was decided to not include them in the analysis. Additionally, in Ref [4] it is shown that the density of doubly-charged ions under these conditions is at least one order of magnitude smaller that that of singly-charged ions.

Acronyms are specified for the different simulations. Starting from EXT simulation, all simplifications except the fifth one above-mentioned, results in simulation I2. Eliminating doubly-charged ions from the study results in the reference simulation (REF) setup, with truncated domain as shown in Fig. 1. The truncated meshes resulted in 880 PIC-mesh elements and 807 MFAM elements (see Tab. 1).

It was verified that such simplifications did not affect considerably the overall performances of the simulation, neither the plasma properties. Table 3 shows the different figures of merit and thruster performances measured for the different simulation cases. The slight mismatch in performances between cases and REF are attributed mainly to the difference of simulated plume extension. Figure 10 shows a comparison between the plasma properties of the EXT and REF simulations. Profiles of the plasma density, electrostatic field, and electron temperature are shown.

ACKNOWLEDGEMENTS

The authors want to thank the developers of Hyphen, in particular A. Domínguez-Vázquez and J. Zhou. The initial research leading to these results has received funding from the European Union H2020 Program under grant agreement number 730028 (Project MINOTOR). The final part of this work was supported by the PROMETEO project, funded by the Comunidad de Madrid, under Grant reference Y2018/NMT-4750 PROMETEO-CM. Part of A. Sánchez-Villar funding came from Spain's Ministry of Science, Innovation and Universities FPU scholarship program with grant FPU17/06352.

REFERENCES

[1] Crimi, G., Eckert, A., and Miller, D., "Microwave Driven Magnetic Plasma Accelerator Studies (Cyclops)," Tech. rep., General Electric Company, Space Sciences Laboratory, Missile and Space Division, 1967.

[2] Sercel, J., "Electron-cyclotron-resonance (ECR) plasma acceleration," *AIAA 19th Fluid Dynamics, Plasma Dynamics and Lasers Conference*, 1987.

[3] Jarrige, J., Elias, P., Cannat, F., and Packan, D., "Characterization of a coaxial ECR plasma thruster," *44th AIAA Plasmadynamics and Lasers Conference, San Diego*, 2013.

[4] Sánchez-Villar, A., Zhou, J., Merino, M., and Ahedo, E., "Coupled plasma transport and electromagnetic wave simulation of an ECR thruster," *Plasma Sources Science and Technology*, submitted for publication.

[5] Jarrige, J., Elias, P., Cannat, F., and Packan, D., "Performance comparison of an ECR plasma thruster using argon and xenon as propellant gas," *33rd International Electric Propulsion Conference*, Paper 2013-420, Electric Rocket Propulsion Society, Fairview Park, OH, Washington D.C., October 7-10, 2013.

[6] Cannat, F., Jarrige, J., Elias, P., and Packan, D., "Experimental investigation of magnetic gradient influence in a coaxial ECR plasma thruster," *Space Propulsion Conference, Cologne, Germany*, 2014.

[7] Cannat, F., Jarrige, J., Lafleur, T., Elias, P., and Packan, D., "Experimental geometry investigation of a coaxial ECR plasma thruster," *Proc. of the 34th Int. Electric Propulsion Conf.(Kobe-Hyogo, Japan)*, 2015, pp. 2015–242.

[8] Cannat, F., Lafleur, T., Jarrige, J., Chabert, P., Elias, P., and Packan, D., "Optimization of a coaxial electron cyclotron resonance plasma thruster with an analytical model," *Physics of Plasmas*, Vol. 22, No. 5, 2015, pp. 053503.

[9] Lafleur, T., Packan, D., Cannat, F., Jarrige, J., and Elias, P., "Modelling of magnetic nozzle thrusters with application to ECR and Helicon thrusters," *34th International Electric Propulsion Conference*, paper 2015-359, Electric Rocket Propulsion Society, Fairview Park, OH, Kobe, Japan, July 6-10, 2015.

[10] Vialis, T., Jarrige, J., Aanesland, A., and Packan, D., "Direct thrust measurement of an electron cyclotron resonance plasma thruster," *Journal of Propulsion and Power*, Vol. 34, No. 5, 2018, pp. 1323–1333.

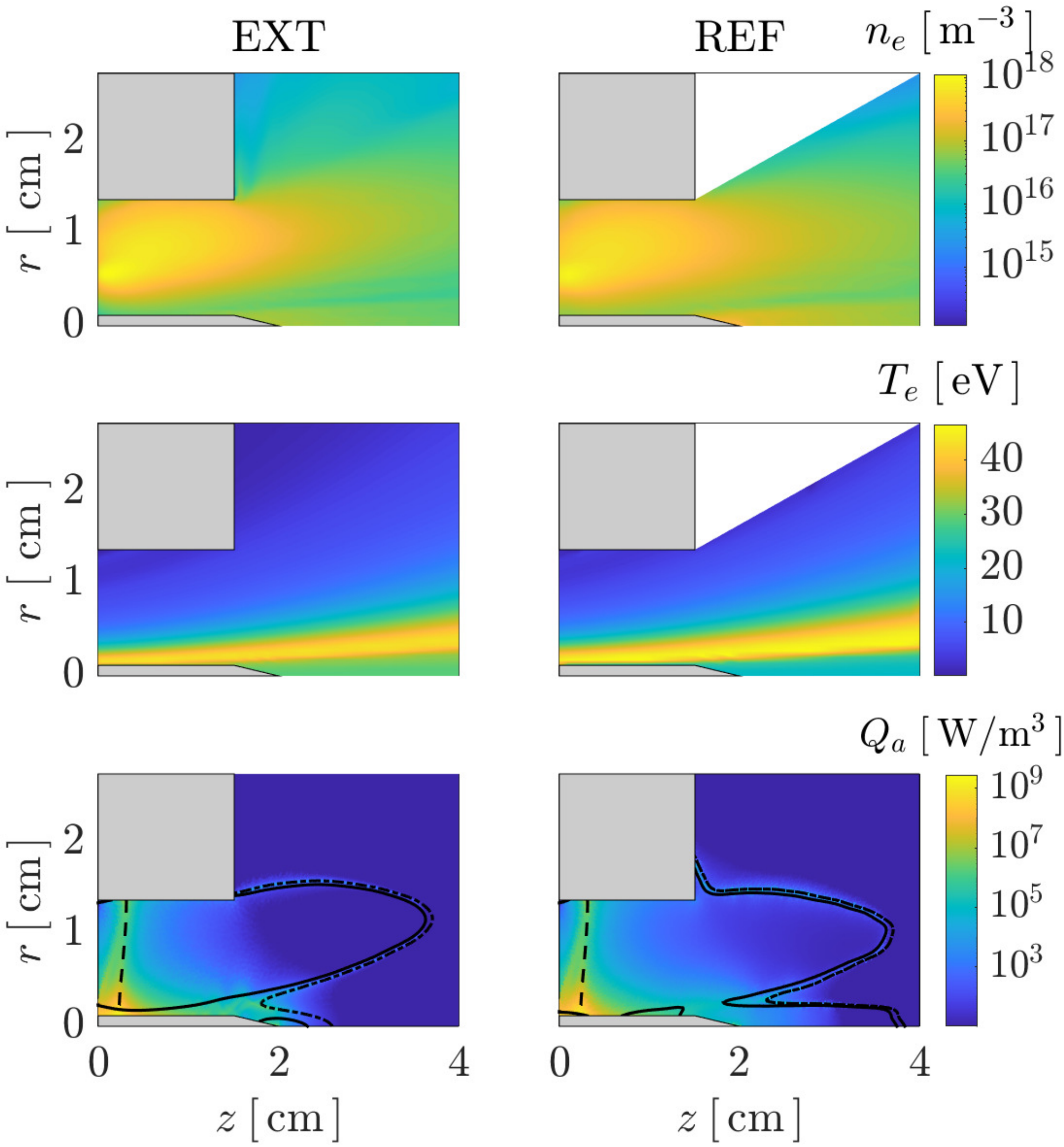

Figure 10: Validation of the stationary values achieved for the electron density, temperature and power absorbed density for cases EXT (left column) and REF (right column).

[11] Correyero, S., Merino, M., Elias, P.-Q., Jarrige, J., Packan, D., and Ahedo, E., "Characterization of diamagnetism inside an ECR thruster with a diamagnetic loop," *Physics of Plasmas*, Vol. 26, No. 5, 2019, pp. 053511.

[12] Peterschmitt, S. and Packan, D., "Comparison of Waveguide Coupled and Coaxial Coupled ECRA Magnetic Nozzle Thruster using a Thrust Balance," *Proc. of the 36th Int. Electric Propulsion Conf.(Vienna, Austria)*, 2019, pp. 2019–188.

[13] Domínguez-Vázquez, A., *Axisymmetric simulation codes for Hall effect thrusters and plasma plumes*, Ph.D. thesis, Universidad Carlos III de Madrid, Leganés, Spain, 2019.

[14] Zhou, J., Pérez-Grande, D., Fajardo, P., and Ahedo, E., "Numerical treatment of a magnetized electron fluid within an electromagnetic plasma thruster code," *Plasma Sources Science and Technology*, Vol. 28, No. 11, 2019, pp. 115004.

[15] Stix, T. H., *Waves in plasmas*, Springer Science & Business Media, 1992.

[16] Correyero, S., Jarrige, J., Packan, D., and Ahedo, E., "Plasma beam characterization along the magnetic nozzle of an ECR thruster," *Plasma Sources Science and Technology*, Vol. 28, No. 9, 2019, pp. 095004.

[17] Merino, M., Sánchez-Villar, A., Ahedo, E., Bonoli, P., Lee, J., Ram, A., and Wright, J., "Wave Propagation and Absorption in ECR Plasma Thrusters," 35^{th} *International Electric Propulsion Conference*, No. IEPC-2017-105, Electric Rocket Propulsion Society, Atlanta, GA, 2017.

Parameter	Name	Units	EXT.	I2.	REF.	M0	M2	P0	P2	ECR0	ECR2	INJZ0	INJR	ON.51W [3]	ON.29W [3]
$\dot{m}$	Mass flow rate	mg/s	0.2	0.2	0.2	**0.15**	**0.25**	0.2	0.2	0.2	0.2	0.2	0.2	0.2	0.2
P_f	Forward power	W	30	30	30	30	30	**15**	**45**	30	30	30	30	51 [1]	29 [1]
B_{factor}	B_0 scaling factor	[-]	1	1	1	1	1	1	1	**0.8**	**1.25**	1	1	1	1
$\boldsymbol{z}_{inj}$	Injector center z	[cm]	0.0	0.0	0.0	0.0	0.0	0.0	0.0	0.0	0.0	0.0	**0.4**	-	-
$\boldsymbol{r}_{inj}$	Injector center r	[cm]	0.5735	0.5735	0.5735	0.5735	0.5735	0.5735	0.5735	0.5735	0.5735	**0.35**	**1.375**	-	-
$\boldsymbol{n}_{inj}$	Injector surface normal	[-]	$\mathbf{1}_z$	$\mathbf{1}_z$	$\mathbf{1}_z$	$\mathbf{1}_z$	$\mathbf{1}_z$	$\mathbf{1}_z$	$\mathbf{1}_z$	$\mathbf{1}_z$	$\mathbf{1}_z$	$\mathbf{1}_z$	$-\mathbf{1}_r$	$\mathbf{1}_z$	$\mathbf{1}_z$
η_c	Coupling efficiency	%	91.8	92.6	91.1	96.1	80.0	87.6	91.6	18.1	98.2	64.5	68.5	–	–
P_a	Absorbed power	W	26.9	27.8	27.3	28.8	24.0	13.1	41.2	5.42	29.5	19.3	20.6	32.2 [1]	18.3 [1]
F	Thrust	mN	0.840	0.741	0.728	0.530	0.781	0.479	0.827	0.238	0.720	0.631	0.713	0.850	0.420
F_i	Ion thrust	mN	0.611	0.496	0.489	0.349	0.515	0.296	0.564	0.124	0.485	0.421	0.490	-	-
F_e	Electron thrust	mN	0.162	0.186	0.169	0.125	0.193	0.120	0.197	0.050	0.173	0.139	0.149	-	-
F_n	Neutral thrust	mN	0.067	0.059	0.070	0.056	0.073	0.063	0.066	0.064	0.062	0.070	0.073	-	-
I_{sp}	Specific impulse	s	428	378	371	360	319	244	422	122	367	322	364	429	214
I_i	Ion current	A	0.082	0.087	0.071	0.049	0.09	0.055	0.08	0.03	0.076	0.068	0.074	0.062	0.036
η_F	Thrust efficiency	%	6.6	5.3	4.9	3.2	5.1	4.4	4.1	2.7	4.4	5.1	6.2	5.6 [1]	2.4 [1]
η_{prod}	Production efficiency	%	40.9	44.2	40.8	40.6	44.5	47.4	39.6	54.6	46.6	42.5	39.1	–	–
η_u	Utilization efficiency	%	50.0	53.0	49.0	44.0	49.0	37.5	54.5	20.1	52.0	46.0	50.5	45.1	25
η_e	Energy efficiency	%	25.3	22.9	22.5	16.5	23.2	23.7	17.8	23.4	19.2	22.0	24.9	16	-
η_{conv}	Conversion efficiency	%	32.2	25.1	25.9	26.3	25.2	25.6	25.3	28.4	26.0	28.2	28.6	-	-
η_d	Divergence efficiency	%	91.2	85.8	84.1	80.4	84.8	80.6	85.3	61.3	83.3	85.3	86.8	70	70
ϵ_{exc}	Excitation losses	%	4.8	4.9	5.1	2.7	7.1	7.2	3.5	9.1	4.3	7.3	8.8	–	–
ϵ_{ion}	Ionization losses	%	7.0	7.1	7.7	5.0	10.1	10.6	5.9	12.2	6.6	9.8	11.2	–	–
ϵ_{wall}	Wall losses	%	63.0	65.4	67.3	76.4	60.1	59.2	73.5	59.4	70.5	62.4	56.9	–	–

Table 3: Outline of cases studied in the presented parametric investigation, including operational parameters, electromagnetic performances, thruster performances and losses conspectus.